Spin dynamics and field-induced magnetic phase transition in the honeycomb Kitaev magnet α-Li_2IrO_3

Sungkyun Choi,[1,*] S. Manni,[2,†] J. Singleton,[3] C. V. Topping,[1,3] T. Lancaster,[4] S. J. Blundell,[1] D. T. Adroja,[5,6] V. Zapf,[3] P. Gegenwart,[2] and R. Coldea[1]

[1]*Clarendon Laboratory, University of Oxford Physics Department, Parks Road, Oxford, OX1 3PU, United Kingdom*
[2]*EP VI, Center for Electronic Correlations and Magnetism, Augsburg University, D-86159 Augsburg, Germany*
[3]*National High Magnetic Field Laboratory MPA-NHMFL, TA-35, MS-E536 Los Alamos National Laboratory, Los Alamos, New Mexico 87545, USA*
[4]*Department of Physics, Durham University, South Road, Durham, DH1 3LE, United Kingdom*
[5]*ISIS Facility, Rutherford Appleton Laboratory-STFC, Chilton, Didcot, OX11 0QX, United Kingdom*
[6]*Highly Correlated Matter Research Group, Physics Department, University of Johannesburg, Auckland Park 2006, South Africa*

(Received 4 October 2018; revised manuscript received 20 January 2019; published 25 February 2019)

The layered honeycomb iridate α-Li_2IrO_3 displays an incommensurate magnetic structure with counter-rotating moments on nearest-neighbor sites, proposed to be stabilized by strongly frustrated anisotropic Kitaev interactions between spin-orbit entangled Ir^{4+} magnetic moments. Here we report powder inelastic neutron scattering measurements that observe sharply dispersive low-energy magnetic excitations centered at the magnetic ordering wave vector, attributed to Goldstone excitations of the incommensurate order, as well as an additional intense mode above a gap $\Delta \simeq 2.3$ meV. Zero-field muon-spin relaxation measurements show clear oscillations in the muon polarization below the Néel temperature $T_N \simeq 15$ K with a time-dependent profile consistent with bulk incommensurate long-range magnetism. Pulsed-field magnetization measurements observe that only about half the saturation magnetization value is reached at the maximum field of 64 T. A clear anomaly near 25 T indicates a transition to a phase with reduced susceptibility. The transition field has a Zeeman energy comparable to the zero-field gapped mode, suggesting gap suppression as a possible mechanism for the field-induced transition.

DOI: 10.1103/PhysRevB.99.054426

I. INTRODUCTION

The cooperative magnetism of 4*d* and 5*d* transition metal ions with strong spin-orbit coupling is attracting much interest as a platform to potentially realize unconventional magnetic states stabilized by strong frustration effects from bond-dependent anisotropic couplings [1–3]. A canonical Hamiltonian in this context is the Kitaev model on the honeycomb lattice [4] with orthogonal moment components coupled via Ising interactions along the three bonds emerging out of each site. This leads to strong frustration effects that stabilize a quantum spin liquid ground state with exotic quasiparticles [5]. Potential hosts of Kitaev physics are tri-coordinated lattices of $5d^5$ Ir^{4+} or $4d^5$ Ru^{3+} ions inside edge-sharing octahedra, where spin-orbit entangled $J_{\text{eff}} = 1/2$ moments (stabilized by spin-orbit coupling and cubic crystal field) are expected to interact to leading order via Ising couplings [6]. Candidate materials to realize such interactions include the layered honeycomb Na_2IrO_3 [7], α-$RuCl_3$ [8], and α-Li_2IrO_3 [9], as well as the three-dimensional structural polytypes β-Li_2IrO_3 [10] and γ-Li_2IrO_3 [11] with hyperhoneycomb and stripy-honeycomb magnetic lattices, respectively. The current understanding is that all the above materials have strong Kitaev exchanges, but additional subleading interactions also present are sufficient to instead stabilize magnetic order: zigzag antiferromagnetism for Na_2IrO_3 [12–16] and α-$RuCl_3$ [17,18], and incommensurate counter-rotating structures for the Li_2IrO_3 family [19–21]. Promising avenues explored to suppress long-range magnetic order are hydrogen intercalation in $H_3LiIr_2O_6$ [22] and high-pressure studies of β-Li_2IrO_3 [23–26] and γ-Li_2IrO_3 [27].

The most detailed spin dynamics studies are available for α-$RuCl_3$, where inelastic neutron scattering experiments observe strong scattering continua indicative of large quantum fluctuations coexisting with magnetic order [28,29]. Dispersive magnetic excitations have also been observed in Na_2IrO_3 via neutron scattering [13] and resonant inelastic x-ray scattering [30], but the spin dynamics in the Li_2IrO_3 family has not been reported so far. Here we present first inelastic neutron scattering measurements of the spin dynamics in the α polytype. All three polytypes display closely related incommensurate counter-rotating magnetic structures, where magnetic moments rotate between adjacent unit cells in the direction of propagation, but rotate in opposite senses for nearest-neighbor sites (see Fig. 5 of [19]); the counter-rotation cannot be explained by Heisenberg-type interactions and provides direct evidence for the presence of dominant

*Present address: Rutgers Center for Emergent Materials and Department of Physics and Astronomy, Rutgers University, Piscataway, New Jersey 08854, USA.
†Present address: Indian Institute of Technology Palakkad, Kerala, India.

bond-dependent anisotropic couplings [31–33]. The excitations of incommensurate counter-rotating structures are of fundamental conceptual interest because conventional spin-wave approaches are inapplicable [34,35]. The standard approach of finding the spin-wave spectrum of rotating structures is to rewrite the problem in a local reference frame that follows the rotation of the equilibrium spin direction. For corotating structures (moments on all sites rotate in the same sense) the resulting spin-wave Hamiltonian has the periodicity of the lattice and the spectrum can be easily found. However, for incommensurate counter-rotating structures the spin-wave Hamiltonian in the rotating frame is not periodic between adjacent unit cells, it repeats only over an infinitely many structural cells and the theoretical spectrum is known only in a few special cases [34].

Another potential route to observe novel effects due to strong Kitaev interactions is in the behavior in high applied magnetic fields. It is notable that α-$RuCl_3$ [17,36] and β-Li_2IrO_3 [10,37], and potentially also γ-Li_2IrO_3 [38], show suppression of the spontaneous magnetic order at relatively low applied magnetic fields when compared to the dominant magnetic interaction strength, suggesting that strong quantum fluctuations, potentially enhanced by the proximity to a nearby spin-liquid phase in parameter space, play an important role in the suppression of the magnetic order. The mechanism of the field-induced transition and the properties above the critical field in those Kitev materials are currently attracting much interest, both experimentally as well as theoretically [39–42].

Here we extend the investigation of the magnetic behavior of α-Li_2IrO_3 by exploring the magnetic phase diagram up to 64 T. This reveals a field-induced transition near 25 T to another magnetic phase with reduced susceptibility and magnetization still much smaller than the expected saturated value. We also report measurements of the spin dynamics over a wide energy range using time-of-flight inelastic neutron scattering with an optimized setup to minimize neutron absorption. At low temperatures in the magnetically ordered phase we observe a clear dispersive inelastic magnetic signal centered at the magnetic ordering wave vector, gapless within the experimental resolution and attributed to Goldstone mode fluctuations of the incommensurate magnetic order. In addition, we also find an intense gapped mode, which may be due to fluctuations out of the moment rotation plane. The gapped mode energy is comparable to the Zeeman energy of the transition field observed in the pulsed-field magnetization data, suggesting gap suppression as a possible mechanism of the field-induced transition.

The paper is organized as follows. We first present in Secs. II–III magnetic susceptibility and muon-spin relaxation measurements of powder α-Li_2IrO_3 samples that confirm the presence of a sharp magnetic transition near 15 K to a well-defined, long-range magnetic order, which pervades the bulk of the samples. Section IV shows measurements of the spin dynamics via powder inelastic neutron scattering, with the data parametrized in Sec. V in terms of two magnetic excitations, a linearly dispersive, gapless mode and an additional quadratic mode above a finite energy gap. Section VI presents magnetization measurements in pulsed fields, which observe a clear anomaly indicative of a magnetic transition at a critical field of Zeeman energy comparable to the zero-field gapped mode energy. Section VII discusses the results in the context of the expected mean-field phase diagram of incommensurate spiral-ordered magnets in applied field and the empirical magnetic phase diagram of other Kitaev magnets. Finally, Sec. VIII summarizes the main results and conclusions.

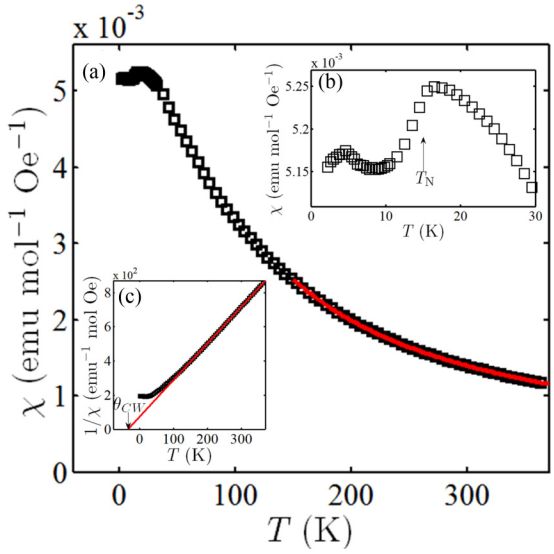

FIG. 1. (a) Temperature dependence of the magnetic susceptibility in powder samples of α-Li_2IrO_3 (zero-field cooled, measurement field $\mu_0 H = 1000$ Oe). The red solid line is a fit to a Curie-Weiss form as discussed in the text. (b) Expansion of the low-temperature region showing a clear anomaly at the magnetic ordering transition near 15 K. (c) Inverse susceptibility fitted to a Curie-Weiss form (red solid line) over the range 150–370 K.

II. MAGNETIC SUSCEPTIBILITY

Magnetic susceptibility measurements were performed using a Quantum Design SQUID magnetometer in the Clarendon Laboratory in Oxford on a fine powder sample (56.5 mg) of α-Li_2IrO_3 synthesized as described elsewhere [9]. The obtained temperature dependence of the susceptibility is shown in Fig. 1(a). The high-temperature region ($150 < T < 370$ K) can be well described (red solid line) by a Curie-Weiss form $\chi = \chi_0 + C/(T + \Theta_{CW})$, with a fixed temperature-independent contribution $\chi_0 = 4.286 \times 10^{-4}$ emu mol^{-1} Oe^{-1}, $C = 0.465$ emu K mol^{-1} Oe^{-1}, and Curie-Weiss temperature $\Theta_{CW} = -33.8$ K, consistent with previous reports [9]. The extracted effective magnetic moment $\mu_{eff} = 1.93\mu_B$ is close to the value $1.73\mu_B$ expected for $J_{eff} = 1/2$ magnetic moments with g factor $g = 2$. Figure 1(b) focuses on the low-temperature behavior where a clear drop in susceptibility is observed near $T_N = 15$ K, characteristic of the onset of long-range magnetic order with antiferromagnetic correlations. We will show later that below this temperature, muon-spin relaxation measurements show evidence of static local magnetic fields. The data also showed a small hump ($\simeq$0.4% change in susceptibility) near 5 K apparent in Fig. 1(b), this is most likely extrinsic as it is not present in susceptibility data on high-purity single crystals [43]. It could be due to the magnetic response of a small impurity phase

present in the powder sample, or be related to the magnetic behavior of spins near faults in the honeycomb layer stacking sequence; it is known that the occurrence of stacking faults in those materials can depend sensitively on the synthesis conditions [44].

III. MUON-SPIN RELAXATION

To further characterize the magnetic order zero-field muon-spin relaxation (ZF μ^+SR), measurements were performed on powder samples from the same batch using the general purpose surface-muon instrument (GPS) at the Swiss Muon Source (SμS), Paul Scherrer Institut, Villigen, Switzerland. In a μ^+SR experiment [45] spin polarized muons are implanted into the sample. The quantity of interest is the asymmetry $A(t)$, which is proportional to the spin polarization of the muon ensemble.

Figure 2(a) shows representative ZF μ^+SR spectra. Below $T_N = 15$ K, a heavily damped oscillation in the muon asymmetry with a single frequency ν was found, characteristic of long-range magnetic order. The measured data could be fitted for all $T < 15$ K with the function

$$A(t) = A_0 + A_1 e^{-\lambda t}\cos(2\pi\nu t + \phi) + A_2 e^{-(\Lambda t)^{\delta}}. \quad (1)$$

Here the first term, A_0, is a nonrelaxing component accounting for a small fraction of muons that stop in the sample mount along with those muons whose spin components lie along the direction of the quasistatic local magnetic field. The second term, A_1, is the oscillating component and the last term, A_2, is a purely relaxing component, which becomes more prominent upon increasing temperature at the expense of the oscillating component. A nonzero phase $\phi = -\pi/4$ was found to best fit the data. It is notable that this value is often indicative of an incommensurate magnetic ordering [46] in agreement with resonant x-ray and neutron diffraction measurements, which observe the onset below T_N of a moment rotating structure with an incommensurate propagation vector [19]. For the fits, the total relaxing amplitude (at $t = 0$) was kept fixed at 26.6% and the relaxation rate of the oscillations was found to take a constant value of $\lambda = 7.0$ MHz.

The temperature dependence of the extracted oscillation frequency is plotted in Fig. 2(b) and is well described by the phenomenological function $\nu(T) = \nu(0)[1 - (T/T_N)^{\alpha}]^{\beta}$, with $\nu(0) = 2.39(2)$ MHz, $\alpha = 2.5$, $\beta = 0.35(2)$, and $T_N = 15.0(1)$ K. The overall temperature dependence is consistent with the magnetic order parameter extracted from neutron diffraction [open squares in Fig. 2(b)], corresponding to $\sqrt{I}$, where I is the magnetic Bragg peak intensity [19]. The onset temperature is consistent with the location of the sharp anomaly observed in the susceptibility data in Fig. 1(b). The amplitudes of the components that reflect long-range magnetic order (A_0 and A_1) are generally seen to decrease upon increasing temperature, with the purely relaxing component A_2 increasing in their place [see Fig. 2(c)], which is indicative of magnetically disordered regions increasing in volume within the sample as the temperature rises. At the lowest temperature, the data confirm long-range order throughout the sample. The value of $\nu(0)$ is similar to that of the dominant precession frequency recently measured in the β phase of this compound [24]. We note that the relaxation rate Λ of the purely relaxing component appears to have a maximum near 4.7 K [see Fig. 2(d)], which coincides with the presence of a small anomaly in the susceptibility data [see Fig. 1(b)]. Figure 1(e) shows the behavior of the stretching factor δ of the purely relaxing component, which takes a constant value of 1 below 9 K, suggesting a dynamically fluctuating magnetic environment [47]. The parameter δ increases steadily from 1 to 2 on warming in the range $9 \leqslant T \leqslant 12$ K, suggesting that the activation of additional relaxation channels causes the relaxation to become rapid compared to the muon-response time window such that electronic fluctuations are motionally narrowed from the spectra. The consequence is relaxation resulting from quasistatic nuclear moments at high temperature. This scenario is confirmed by the high temperature value of $\Lambda \approx 0.3$ MHz along with measurements made in applied magnetic fields for $T > T_N$, where fields of 5 mT are seen to quench the muon response.

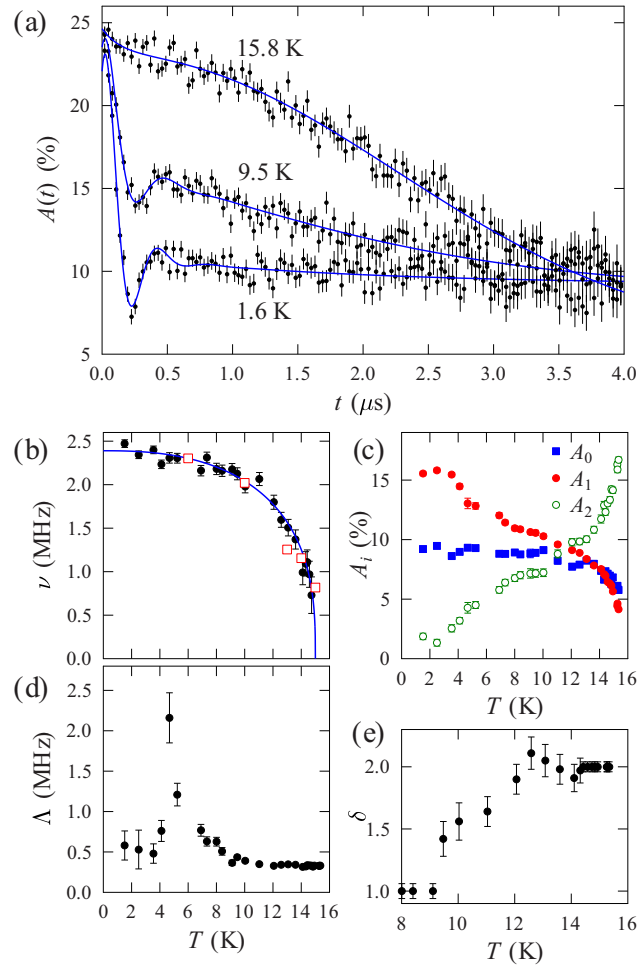

FIG. 2. Muon-spin relaxation results on α-Li_2IrO_3 powder. (a) Representative zero-field μ^+SR spectra measured at several temperatures. Solid lines show fits to the functional form (1) described in the text. (b) Extracted temperature dependence of the muon precession frequency ν (filled circles) fitted to an order parameter behavior (solid line); open squares show the (scaled) order parameter extracted from the intensity of the magnetic Bragg peak observed in neutron powder diffraction data [squares from Fig. 4 (inset) in [19]]. (c) Temperature dependence of the fitted amplitudes A_0, A_1, and A_2. (d) Relaxation rate Λ and (e) stretching factor δ.

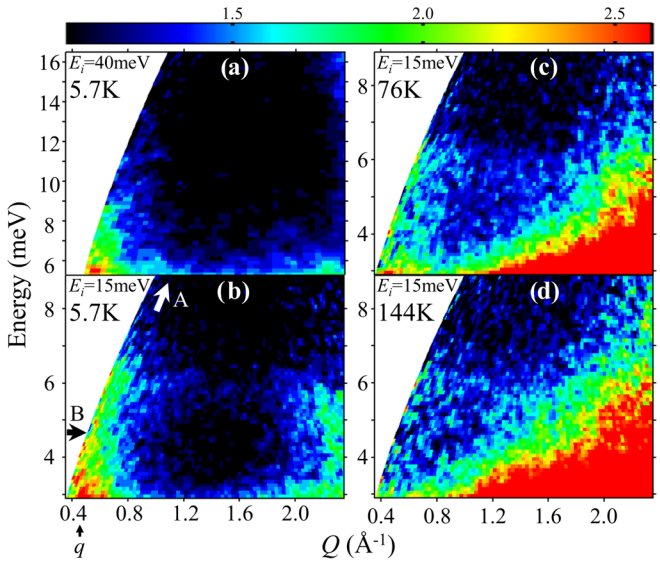

FIG. 3. Powder inelastic neutron scattering intensity as a function of wave vector and energy transfer. A dispersive inelastic signal centered near the magnetic Bragg peak wave vector q (thick vertical arrow below the lower left corner) is clearly observed at 5.7 K deep in the magnetically ordered phase [in (a) and (b)], and becomes damped out at high temperatures [(c) and (d)], as expected for a magnetic inelastic signal. The thick arrows labeled A and B in (b) show directions along which the measured intensities are plotted in Fig. 5(A) and 5(B). Data were collected with $E_i = 40$ meV in (a) and 15 meV in (b)-(d). An overall scale factor was applied to the intensities in (a) to match those in (b) in the overlapping region.

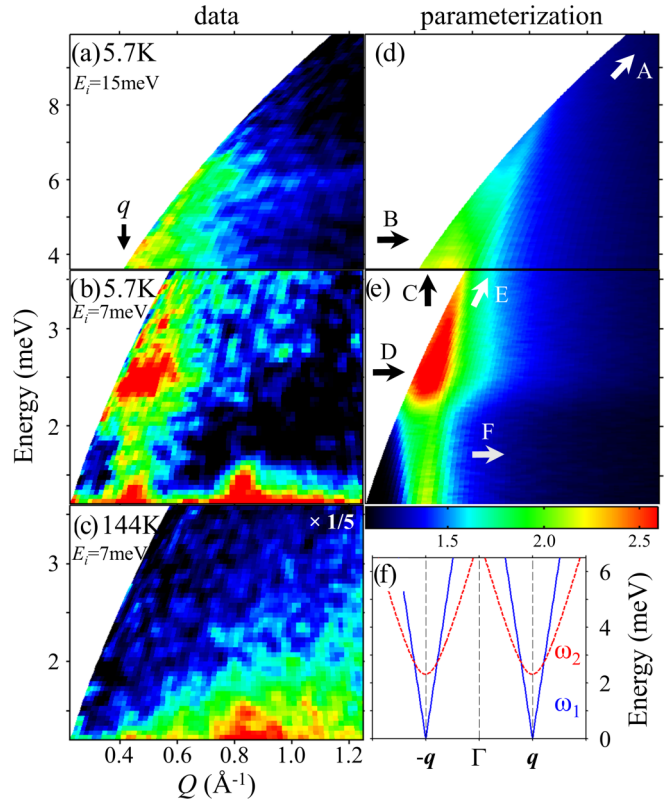

FIG. 4. (a), (b) Higher resolution measurements of the low-energy inelastic neutron scattering intensity. Near the magnetic ordering wave vector q down [thick vertical arrow in (a)], an inelastic signal is observed down to the lowest accessible energy $\simeq 1$ meV with a clear intensity increase near 2.3 meV; all this structure disappears upon heating to high temperatures (c), verifying its magnetic character. Intensities in (c) have been scaled by a factor 1/5 to make them comparable to the other panels. Data in (a) and (b) were collected under different instrumental conditions, and for ease of visualization are shown as if they had a continuous energy axis between them with the intensities in the top panel multiplied by a single overall scale factor to best match those in the lower panel in the overlapping region. (d), (e) Calculated spherically averaged magnetic inelastic scattering intensity (to be compared with the data in (a) and (b) for the model cross section discussed in the text with two modes with dispersions plotted in (f). Thick arrows labeled A–F in (d) and (e) show directions along which the measured and calculated intensities are plotted in Figs. 5(A)–5(F).

IV. POWDER INELASTIC NEUTRON SCATTERING

To probe the spin dynamics, inelastic neutron scattering measurements were performed using the high-flux, time-of-fight, direct-geometry chopper spectrometer MERLIN at ISIS. A fine powder of α-Li_2IrO_3 (8.9 g) was placed in an annular can to minimize the strong neutron absorption from both Ir and Li (absorption cross sections of 425 and 70.5 barns, respectively, for thermal neutrons). Cooling was provided by a closed-cycle refrigerator with a base temperature of 5.7 K, well below T_N. The inelastic scattering was measured for incident neutrons of energies $E_i = 7$, 15, 40, and 80 meV, and a clear inelastic magnetic signal was detected at low wave-vector transfers for energies extending up to 12 meV. Most data were therefore collected with $E_i = 7$ and 15 meV for which the instrumental energy resolution on the elastic line (FWHM) was 0.58(1) and 1.08(1) meV, respectively. Counting times per setting ranged between 17 and 25 h at an average proton current of 150 μA.

Figure 3 shows the wave vector Q and energy E dependence of the inelastic scattering at several temperatures. At low temperatures [Fig. 3(b)] a clear inelastic signal is visible at low wave vectors extending up in energy to at least 7 meV and centered at low energies near the magnitude q (vertical arrow under the figure) of the incommensurate magnetic ordering wave vector $\boldsymbol{q} = (0.32(1), 0, 0)$ [19]. The scattering intensity in this region decreases upon increasing temperature [Fig. 3(c)] and is completely damped out deep in the paramagnetic regime [Fig. 3(d)], confirming its magnetic origin. In contrast, the intensity at large wave vectors and low energies strongly increases upon increasing temperature as expected for scattering processes involving phonons. Measurements with a higher incident neutron energy $E_i = 40$ meV confirmed that the magnetic inelastic signal at low Q extends in energy up to at least 12 meV [see Fig. 3(a)]. Higher resolution measurements (collected with $E_i = 7$ meV), focusing on the low-energy part of the spectrum, are shown in Fig. 4(b). Note the inelastic signal at low wave vectors near the magnetic ordering wave vector q (thick vertical arrow above the data) with strong intensity near 2.3 meV and with a clear signal extending below this region, down to the lowest energies probed. All this structured inelastic signal becomes damped out upon heating to 144 K, Fig. 4(c), confirming its magnetic character.

V. PARAMETRIZATION OF LOW-ENERGY SPIN DYNAMICS BY AN EMPIRICAL SPIN-WAVE MODEL

The low-energy inelastic magnetic response shows weak scattering intensity appearing to emerge out of the magnetic Bragg peak wave vector and extending up in energy, followed by an onset of much stronger scattering intensity above a gap. Those features resemble the generic structure of the low-energy spin excitations near the magnetic ordering wave vector in spiral-ordered magnets with easy-plane anisotropy. In that case the low-energy excitations near the ordering wave vector $\boldsymbol{q}$ contain a gapless (Goldstone) mode with a linear dispersion associated with long-wavelength spin oscillations confined to the spiral plane, and a gapped mode associated with fluctuations normal to the spiral plane. Inspired by this generic resemblance we empirically parametrize the low-energy inelastic data in terms of a minimal model with two dispersive modes (gapless $\hbar\omega_1$ and gapped $\hbar\omega_2$). For simplicity we consider both modes dispersing (isotropically) in the reciprocal $\boldsymbol{a}^*\boldsymbol{b}^*$ plane (as expected for magnetically decoupled honeycomb layers in the ab plane), specifically

$$\hbar\omega_1(\boldsymbol{Q}) = v_1|\boldsymbol{Q}_\perp - \boldsymbol{q}|,$$
$$\hbar\omega_2(\boldsymbol{Q}) = \sqrt{v_2^2|\boldsymbol{Q}_\perp - \boldsymbol{q}|^2 + \Delta^2}, \qquad (2)$$

where $\boldsymbol{q}$ is the incommensurate magnetic ordering wave vector (along $\boldsymbol{a}^*$), $\boldsymbol{Q}_\perp$ is the projection of the 3D wave vector $\boldsymbol{Q}$ onto the $\boldsymbol{a}^*\boldsymbol{b}^*$ plane, $v_{1,2}$ are the velocities of the two modes, and Δ is the gap of the second mode. The above definition is for the case when $\boldsymbol{Q}_\perp$ is in the vicinity of $\boldsymbol{q}$. By symmetry, for wave vectors with $\boldsymbol{Q}_\perp$ in the vicinity of $-\boldsymbol{q}$, the same definition (2) applies, but with $\boldsymbol{q}$ replaced by $-\boldsymbol{q}$. For this parametrization, the dispersions along the $-\boldsymbol{q} \to \Gamma \to \boldsymbol{q}$ direction are illustrated in Fig. 4(f). As a minimal model for the neutron scattering cross section we assume an inverse energy intensity dependence (as generic for low-energy antiferromagnetic spin waves), allow for independent intensity prefactors $A_{1,2}$ for the two modes, and also assume that any effects of the intensity polarization dependence of the modes can be captured in a first approximation by a rescaling of the intensity prefactors $A_{1,2}$. Specifically, we assume the intensity dependence

$$I(\boldsymbol{Q}, E) = \left(\frac{g}{2}f(Q)\right)^2\left[\frac{A_1}{E}G(E - \hbar\omega_1(\boldsymbol{Q})) + \frac{A_2}{E}G(E - \hbar\omega_2(\boldsymbol{Q}))\right], \qquad (3)$$

where $f(Q)$ is the Ir^{4+} spherical magnetic form factor [48] the g factor was assumed to be equal to 2 and $G(E)$ is a Gaussian function that reflects the finite instrumental energy resolution.

For comparison with the INS data at a given (Q, E) point the above equation was numerically averaged for a spherical distribution of wave-vector transfers $\boldsymbol{Q}$ of fixed magnitude Q. The above parametrization could capture well the observed intensity dependence of the magnetic scattering in wave vector and energy. Representative values for the model parameters are $A_1/A_2 = 2.7$, $v_1 = 12.2$ meVÅ, $v_2 = 6.5$ meVÅ, and gap $\Delta = 2.3$ meV. The level of agreement obtained in this case can be seen by comparing the data in Figs. 4(a) and 4(b) with the calculations in Figs. 4(d) and 4(e). The intensities in representative scans along energy and momentum directions are shown in Fig. 5(A)–5(F); the trends in the data (filled symbols) are well captured by the empirical parametrization (solid red lines). The constant-energy scan F below the energy gap Δ shows a clear peak in intensity near 0.45 $Å^{-1}$ (which disappears at high temperatures, open squares); this intensity is associated with scattering from the $\hbar\omega_1$ mode. The energy scans C and E are directly sensitive to the gap Δ where a clear increase in scattering intensity is observed. In spite of its simplified nature, the empirical model with two modes with two-dimensional dispersions provides a good description of the general features of the magnetic inelastic scattering data from the lowest measured energies $\simeq 1$ meV up to intermediate energies $\simeq 5$ meV. We also compared the data with a modified model with isotropic 3D dispersions for both modes [with $\boldsymbol{Q}_\perp$ replaced by $\boldsymbol{Q}$ in (2)], but this gave a worse fit to the experimental data, suggesting that a model with predominantly two-dimensional dispersions (as expected for nearly magnetically decoupled layers) is a more suitable description.

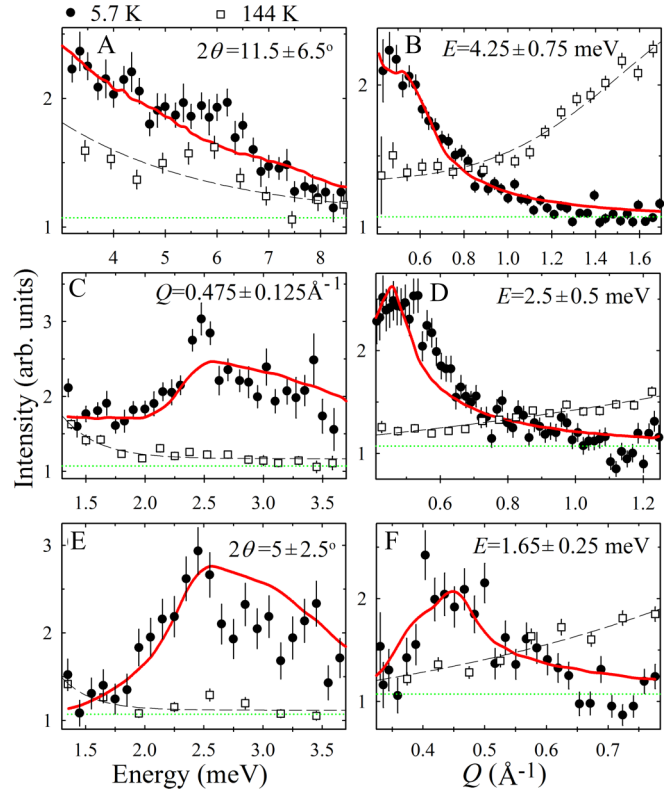

FIG. 5. (A–F) Scans through the inelastic neutron scattering data in Figs. 3(b) and 4(d)–4(e) along directions indicated by the thick arrows labelled (A–F). Filled (open) symbols are data at 5.7 K (144 K) and solid red lines show the corresponding intensities in the empirical model parametrization defined in Eqs. (2) and (3). Dashed lines are guides to the eye to indicate the trends in the 144 K data. Green dotted lines show the estimated nonmagnetic background at low temperatures obtained by extrapolation from regions of high Q or high E. Panel legends give the intensity integration ranges in wave vector Q, energy E, or total scattering angle 2θ.

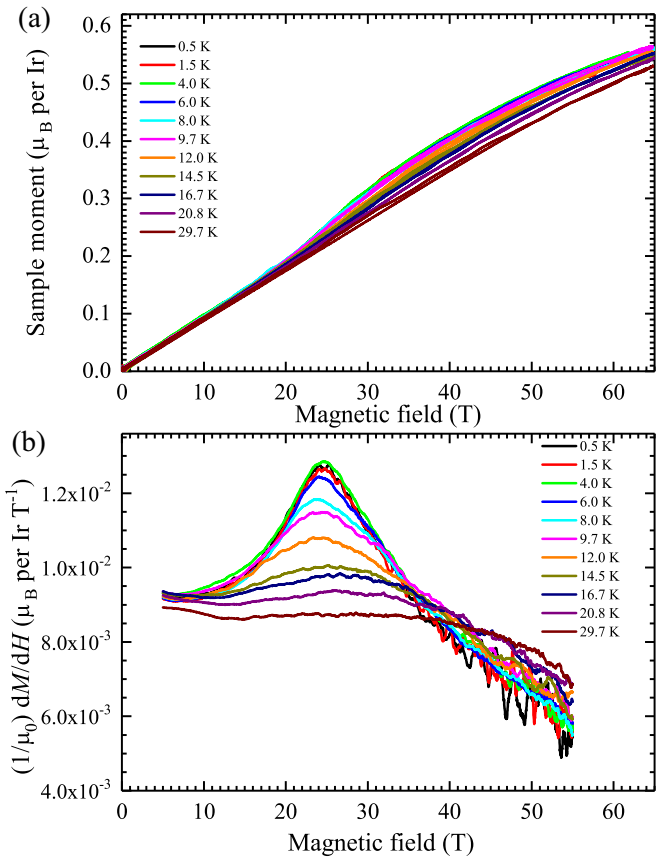

FIG. 6. (a) Magnetization as a function of applied field $\mu_0 H$ for a selection of temperatures. The curves are composites of pulsed-field data (8–64 T, averaged over multiple shots) and low-field VSM data (0–13 T). (b) Differentials of the smoothed data sets in (a).

VI. PULSED-FIELD MAGNETIZATION

Pulsed-field magnetization experiments were performed using the extraction magnetometer described in [49], placed within a ^{3}He cryostat with a base temperature of 0.4 K and the 65 T short-pulse magnet at NHMFL Los Alamos [50]. The magnetization values measured in the pulsed-field experiments were calibrated into absolute units using data collected using a vibrating sample magnetometer (VSM). Magnetic field $M(H, T)$ data are shown for field sweeps up to 64 T at various constant temperatures T in Fig. 6(a). The low-temperature $M(H)$ curves show a pronounced steepening near a critical field $\mu_0 H_C \simeq 25$ T, as characteristic of a field-induced phase transition. Differential susceptibility curves plotted in Fig. 6(b) observe a well-defined "peak" at this field at low temperatures, with the peak decreasing in amplitude and broadening upon increasing temperature, with dramatic broadening above $\simeq 14.5$ K. The differential susceptibility has a clear downward trend upon an increasing field much above the peak. At these high fields, the susceptibility is significantly suppressed compared to the value in the low-field spiral ordered region, but the absolute magnetization value is still only about half the expected saturation, assuming a g factor 2. Using the same g factor, the Zeeman energy of the critical field is $\simeq 2.9$ meV, comparable to the energy of the gapped mode in zero field ($\Delta \simeq 2.3$ meV), suggesting that the mechanism of the phase transition could be related to the applied field suppressing this energy gap.

VII. DISCUSSION

It is interesting to set in context the magnetic phase transition observed near 25 T in α-Li_2IrO_3. The behavior of incommensurate spiral ordered magnets in a magnetic field has been mostly investigated experimentally and theoretically (via mean-field analysis) for systems with frustrated isotropic, Heisenberg-type interactions and some weak easy-plane anisotropy [51]. In this case for fields applied normal to the rotation plane the moments cant toward the field direction to form a cone, typically stable up to the transition to magnetic saturation. For fields applied in the plane of rotation a succession of distinct phases is expected upon increasing field: spiral → cone → fan → saturated paramagnet; the first transition occurs at a field that overcomes a relatively small in-plane anisotropy energy, when the plane of moment rotation "flops" to be normal to the field axis and moments cant toward the field direction to form a cone. Those transitions would be detectable via anomalies in the magnetization curve as a function of field and for a powder sample, one would expect to observe the spherical average of the magnetization curve for all possible directions of the applied field.

Interpreting the measurements on α-Li_2IrO_3 in the above scenario, the transition at 25 T would be identified with the flopping of the moment rotation plane to become normal to the field axis with moments canted to form a cone phase; this transition would occur in the powder grains oriented to have the spin spiral almost parallel to the field direction with the grains oriented with the spiral plane near normal to the field expected to have a smooth behavior.

However, one difficulty with the above interpretation is that the susceptibility is seen experimentally to significantly decrease upon increasing the field above the transition, see Fig. 6(b), whereas a near-constant susceptibility would be expected at the mean-field level throughout the cone phase (almost independent of the field orientation). Also, the type of spiral order observed in α-Li_2IrO_3 with counter-rotating moments cannot be stabilized by Heisenberg-type interactions. In contrast, dominant (ferromagnetic) strongly anisotropic Kitaev terms are required [19] and in such cases the magnetic phase diagram in the applied field could be qualitatively different, as suggested by recent theoretical proposals for three-dimensional hyperhoneycomb Kitaev magnets [35,52]. Experimental studies of other Kitaev materials such as α-$RuCl_3$ [17,36], β-Li_2IrO_3 [10,37], and potentially also γ-Li_2IrO_3 [38], showed that relatively modest fields compared to the overall strength of the magnetic exchanges can suppress the spontaneous magnetic order altogether and stabilize instead an extended quantum paramagnetic region with significant quantum fluctuations.

We hope our experimental studies will stimulate further theoretical studies of the magnetic phase diagram of honeycomb Kitaev systems with incommensurate counter-rotating order, which may bring insight into the physics of the field-induced phase transition in α-Li_2IrO_3, the magnetic properties

above the critical field, and the potential role played by the low-energy gapped mode observed in the inelastic neutron scattering data in the mechanism of the field-induced transition. On the experimental side, future high-field magnetometry studies on single crystal samples, which have recently become available [44], could provide important information on the magnetic properties above the critical transition field.

VIII. CONCLUSIONS

To summarize, we have probed the spin dynamics in the layered honeycomb magnet α-Li_2IrO_3, which displays an incommensurate magnetic structure with counter-rotating moments, proposed to be stabilized by frustrated Kitaev interactions. The low-energy magnetic excitation spectrum observed by inelastic neutron scattering could be well parametrized by a gapless mode centered at the magnetic ordering wave vector, associated with Goldstone mode fluctuations of the incommensurate order, and an additional intense gapped mode. In magnetization measurements in pulsed fields we have observed evidence for a field-induced transition near 25 T to another magnetic phase with suppressed magnetic susceptibility and magnetization still well below the expected saturation.

In accordance with the EPSRC policy framework on research data, access to the data will be made available from [53].

ACKNOWLEDGMENTS

We thank Paul Goddard and Itamar Kimchi for very helpful discussions. We are grateful to Alex Amato and Hubertus Luetkens at SμS for experimental assistance. Work at Oxford was supported by the European Research Council (ERC) under the European Union's Horizon 2020 research and innovation program Grant Agreement Number 788814 (EQFT) and by EPSRC (UK) under Grants No. EP/H014934/1, No. EP/M020517/1, and No. EP/N023803/1; at Durham by EPSRC Grants No. EP/G003092/2 and No. EP/N024028/1; and at ISIS by STFC (UK). Work at Augsburg was supported by the Helmholtz Virtual Institute 521 "New states of matter and their excitations" and the German Science Foundation through TRR-80. Work at LANL was supported by the U.S. Department of Energy (DOE) Basic Energy Science Field Work Proposal "Science in 100 T". The NHMFL facility at LANL is funded by the National Science Foundation Cooperative Agreement No. DMR-1157490, the State of Florida, and the U.S. DOE.

[1] J. G. Rau, E. K.-H. Lee, and H.-Y. Kee, Annu. Rev. Condens. Matter Phys. **7**, 195 (2016).
[2] S. M. Winter, Y. Li, H. O. Jeschke, and R. Valentí, Phys. Rev. B **93**, 214431 (2016).
[3] M. Hermanns, I. Kimchi, and J. Knolle, Annu. Rev. Condens. Matter Phys. **9**, 17 (2018).
[4] A. Kitaev, Ann. Phys. (NY) **321**, 2 (2006).
[5] J. Knolle, D. L. Kovrizhin, J. T. Chalker, and R. Moessner, Phys. Rev. Lett. **112**, 207203 (2014).
[6] J. Chaloupka, G. Jackeli, and G. Khaliullin, Phys. Rev. Lett. **110**, 097204 (2013).
[7] Y. Singh and P. Gegenwart, Phys. Rev. B **82**, 064412 (2010).
[8] K. W. Plumb, J. P. Clancy, L. J. Sandilands, V. V. Shankar, Y. F. Hu, K. S. Burch, H.-Y. Kee, and Y.-J. Kim, Phys. Rev. B **90**, 041112 (2014).
[9] Y. Singh, S. Manni, J. Reuther, T. Berlijn, R. Thomale, W. Ku, S. Trebst, and P. Gegenwart, Phys. Rev. Lett. **108**, 127203 (2012).
[10] T. Takayama, A. Kato, R. Dinnebier, J. Nuss, H. Kono, L. S. I. Veiga, G. Fabbris, D. Haskel, and H. Takagi, Phys. Rev. Lett. **114**, 077202 (2015).
[11] K. A. Modic, T. E. Smidt, I. Kimchi, N. P. Breznay, A. Biffin, S. Choi, R. D. Johnson, R. Coldea, P. Watkins-Curry, G. T. McCandless, J. Y. Chan, F. Gandara, Z. Islam, A. Vishwanath, A. Shekhter, R. D. McDonald, and J. G. Analytis, Nat. Commun. **5**, 4203 (2014).
[12] X. Liu, T. Berlijn, W.-G. Yin, W. Ku, A. Tsvelik, Y.-J. Kim, H. Gretarsson, Y. Singh, P. Gegenwart, and J. P. Hill, Phys. Rev. B **83**, 220403 (2011).
[13] S. K. Choi, R. Coldea, A. N. Kolmogorov, T. Lancaster, I. I. Mazin, S. J. Blundell, P. G. Radaelli, Y. Singh, P. Gegenwart, K. R. Choi, S.-W. Cheong, P. J. Baker, C. Stock, and J. Taylor, Phys. Rev. Lett. **108**, 127204 (2012).
[14] F. Ye, S. Chi, H. Cao, B. C. Chakoumakos, J. A. Fernandez-Baca, R. Custelcean, T. F. Qi, O. B. Korneta, and G. Cao, Phys. Rev. B **85**, 180403 (2012).
[15] S. Hwan Chun, J.-W. Kim, J. Kim, H. Zheng, C. C. Stoumpos, C. D. Malliakas, J. F. Mitchell, K. Mehlawat, Y. Singh, Y. Choi, T. Gog, A. Al-Zein, M. M. Sala, J. Krisch, M. Chaloupka, G. Jackeli, G. Khaliullin, and B. J. Kim, Nat. Phys. **11**, 462 (2015).
[16] S. D. Das, S. Kundu, Z. Zhu, E. Mun, R. D. McDonald, G. Li, L. Balicas, A. McCollam, G. Cao, J. G. Rau, H.-Y. Kee, V. Tripathi, and S. E. Sebastian, Phys. Rev. B **99**, 081101(R) (2019).
[17] R. D. Johnson, S. C. Williams, A. A. Haghighirad, J. Singleton, V. Zapf, P. Manuel, I. I. Mazin, Y. Li, H. O. Jeschke, R. Valentí, and R. Coldea, Phys. Rev. B **92**, 235119 (2015).
[18] A. Banerjee, C. A. Bridges, J.-Q. Yan, A. A. Aczel, L. Li, M. B. Stone, G. E. Granroth, M. D. Lumsden, Y. Yiu, J. Knolle, S. Bhattacharjee, D. L. Kovrizhin, R. Moessner, D. A. Tennant, D. G. Mandrus, and S. E. Nagler, Nat. Mater. **15**, 733 (2016).
[19] S. C. Williams, R. D. Johnson, F. Freund, S. Choi, A. Jesche, I. Kimchi, S. Manni, A. Bombardi, P. Manuel, P. Gegenwart, and R. Coldea, Phys. Rev. B **93**, 195158 (2016).
[20] A. Biffin, R. D. Johnson, S. Choi, F. Freund, S. Manni, A. Bombardi, P. Manuel, P. Gegenwart, and R. Coldea, Phys. Rev. B **90**, 205116 (2014).
[21] A. Biffin, R. D. Johnson, I. Kimchi, R. Morris, A. Bombardi, J. G. Analytis, A. Vishwanath, and R. Coldea, Phys. Rev. Lett. **113**, 197201 (2014).
[22] K. Kitagawa, T. Takayama, Y. Matsumoto, A. Kato, R. Takano, Y. Kishimoto, S. Bette, R. Dinnebier, G. Jackeli, and H. Takagi, Nature **554**, 341 (2018).
[23] L. S. I. Veiga, M. Etter, K. Glazyrin, F. Sun, C. A. Escanhoela, G. Fabbris, J. R. L. Mardegan, P. S. Malavi, Y. Deng, P. P. Stavropoulos, H.-Y. Kee, W. G. Yang, M. van Veenendaal,

J. S. Schilling, T. Takayama, H. Takagi, and D. Haskel, Phys. Rev. B **96**, 140402 (2017).
[24] M. Majumder, R. S. Manna, G. Simutis, J. C. Orain, T. Dey, F. Freund, A. Jesche, R. Khasanov, P. K. Biswas, E. Bykova, N. Dubrovinskaia, L. S. Dubrovinsky, R. Yadav, L. Hozoi, S. Nishimoto, A. A. Tsirlin, and P. Gegenwart, Phys. Rev. Lett. **120**, 237202 (2018).
[25] T. Takayama, A. Krajewska, A. S. Gibbs, A. N. Yaresko, H. Ishii, H. Yamaoka, K. Ishii, N. Hiraoka, N. P. Funnell, C. L. Bull, and H. Takagi, arXiv:1808.05494.
[26] S. Choi, H.-S. Kim, H.-H. Kim, A. Krajewska, G. Kim, M. Minola, T. Takayama, K. Haule, D. Vanderbilt, H. Takagi, and B. Keimer (unpublished).
[27] N. P. Breznay, A. Ruiz, A. Frano, W. Bi, R. J. Birgeneau, D. Haskel, and J. G. Analytis, Phys. Rev. B **96**, 020402 (2017).
[28] A. Banerjee, J. Yan, J. Knolle, C. A. Bridges, M. B. Stone, M. D. Lumsden, D. G. Mandrus, D. A. Tennant, R. Moessner, and S. E. Nagler, Science **356**, 1055 (2017).
[29] S.-H. Do, S.-Y. Park, J. Yoshitake, J. Nasu, Y. Motome, Y. S. Kwon, D. T. Adroja, D. J. Voneshen, K. Kim, T.-H. Jang, J.-H. Park, K.-Y. Choi, and S. Ji, Nat. Phys. **13**, 1079 (2017).
[30] H. Gretarsson, J. P. Clancy, Y. Singh, P. Gegenwart, J. P. Hill, J. Kim, M. H. Upton, A. H. Said, D. Casa, T. Gog, and Y.-J. Kim, Phys. Rev. B **87**, 220407 (2013).
[31] I. Kimchi, R. Coldea, and A. Vishwanath, Phys. Rev. B **91**, 245134 (2015).
[32] E. K.-H. Lee and Y. B. Kim, Phys. Rev. B **91**, 064407 (2015).
[33] E. K.-H. Lee, J. G. Rau, and Y. B. Kim, Phys. Rev. B **93**, 184420 (2016).
[34] I. Kimchi and R. Coldea, Phys. Rev. B **94**, 201110 (2016).
[35] S. Ducatman, I. Rousochatzakis, and N. B. Perkins, Phys. Rev. B **97**, 125125 (2018).
[36] J. A. Sears, Y. Zhao, Z. Xu, J. W. Lynn, and Y.-J. Kim, Phys. Rev. B **95**, 180411 (2017).
[37] A. Ruiz, A. Frano, N. P. Breznay, I. Kimchi, T. Helm, I. Oswald, J. Y. Chan, R. J. Birgeneau, Z. Islam, and J. G. Analytis, Nat. Commun. **8**, 961 (2017).
[38] K. A. Modic, B. J. Ramshaw, J. B. Betts, N. P. Breznay, J. G. Analytis, R. D. McDonald, and A. Shekhter, Nat. Commun. **8**, 180 (2017).
[39] A. Banerjee, P. Lampen-Kelley, J. Knolle, C. Balz, A. Aczel, B. Winn, Y. Liu, D. Pajerowski, J.-Q. Yan, C. Bridges, A. Savici, B. Chakoumakos, M. Lumsden, D. Tennant, R. Moessner, D. Mandrus, and S. Nagler, npj Quantum Mater. **3**, 8 (2018).
[40] Y. Kasahara, T. Ohnishi, Y. Mizukami, O. Tanaka, S. Ma, K. Sugii, N. Kurita, H. Tanaka, J. Nasu, Y. Motome, T. Shibauchi, and Y. Matsuda, Nature **559**, 227 (2018).
[41] S. M. Winter, K. Riedl, D. Kaib, R. Coldea, and R. Valentí, Phys. Rev. Lett. **120**, 077203 (2018).
[42] P. Lampen-Kelley, L. Janssen, E. C. Andrade, S. Rachel, J.-Q. Yan, C. Balz, D. G. Mandrus, S. E. Nagler, and M. Vojta, arXiv:1807.06192.
[43] I.-M. Pietsch, A. Jesche, and P. Gegenwart (unpublished).
[44] F. Freund, S. C. Williams, R. D. Johnson, R. Coldea, P. Gegenwart, and A. Jesche, Sci. Rep. **6**, 35362 (2016).
[45] S. J. Blundell, Contemp. Phys. **40**, 175 (1999).
[46] J. Sugiyama, J. H. Brewer, E. J. Ansaldo, B. Hitti, M. Mikami, Y. Mori, and T. Sasaki, Phys. Rev. B **69**, 214423 (2004).
[47] R. S. Hayano, Y. J. Uemura, J. Imazato, N. Nishida, T. Yamazaki, and R. Kubo, Phys. Rev. B **20**, 850 (1979).
[48] J. W. Lynn, G. Shirane, and M. Blume, Phys. Rev. Lett. **37**, 154 (1976).
[49] P. A. Goddard, J. Singleton, P. Sengupta, R. D. McDonald, T. Lancaster, S. J. Blundell, F. L. Pratt, S. Cox, N. Harrison, J. L. Manson, H. I. Southerland, and J. A. Schlueter, New J. Phys. **10**, 083025 (2008).
[50] M. Jaime, A. Lacerda, Y. Takano, and G. S. Boebinger, J. Phys.: Conf. Ser. **51**, 643 (2006).
[51] T. Nagamiya, K. Nagata, and Y. Kitano, Progr. Theor. Phys. **27**, 1253 (1962).
[52] I. Rousochatzakis and N. B. Perkins, Phys. Rev. B **97**, 174423 (2018).
[53] DOI: http://dx.doi.org/10.5287/bodleian:j0xr2EaZK.